



Article

Biomimetic Catalysts Based on Au@TiO₂-MoS₂-CeO₂ Composites for the Production of Hydrogen by Water Splitting

Kenneth Fontánez ¹, Diego García ², Dayna Ortiz ³, Paola Sampayo ³, Luis Hernández ³, María Cotto ³, José Ducongé ³, Francisco Díaz ³, Carmen Morant ⁴ , Florian Petrescu ³ , Abniel Machín ^{5,*} and Francisco Márquez ^{3,*}

¹ Department of Chemistry, University of Puerto Rico, Rio Piedras Campus, San Juan 00925, Puerto Rico

² Department of Biochemistry, School of Medicine, University of Puerto Rico, Medical Sciences Campus, San Juan 00936, Puerto Rico

³ Nanomaterials Research Group, Department of Natural Sciences and Technology, Division of Natural Sciences, Technology and Environment, Universidad Ana G. Méndez-Gurabo Campus, Gurabo 00778, Puerto Rico

⁴ Department of Applied Physics, Autonomous University of Madrid, Instituto de Ciencia de Materiales Nicolás Cabrera, 28049 Madrid, Spain

⁵ Department of Natural Sciences and Technology, Division of Natural Sciences, Technology and Environment, Universidad Ana G. Méndez-Cupey Campus, San Juan 00926, Puerto Rico

* Correspondence: machina1@uagm.edu (A.M.); fmarquez@uagm.edu (F.M.)

Abstract: The photocatalytic hydrogen evolution reaction (HER) by water splitting has been studied, using catalysts based on crystalline TiO₂ nanowires (TiO₂NWs), which were synthesized by a hydrothermal procedure. This nanomaterial was subsequently modified by incorporating different loadings (1%, 3% and 5%) of gold nanoparticles (AuNPs) on the surface, previously exfoliated MoS₂ nanosheets, and CeO₂ nanoparticles (CeO₂NPs). These nanomaterials, as well as the different synthesized catalysts, were characterized by electron microscopy (HR-SEM and HR-TEM), XPS, XRD, Raman, Reflectance and BET surface area. HER studies were performed in aqueous solution, under irradiation at different wavelengths (UV-visible), which were selected through the appropriate use of optical filters. The results obtained show that there is a synergistic effect between the different nanomaterials of the catalysts. The specific area of the catalyst, and especially the increased loading of MoS₂ and CeO₂NPs in the catalyst substantially improved the H₂ production, with values of ca. 1114 µm²/hg for the catalyst that had the best efficiency. Recyclability studies showed only a decrease in activity of approx. 7% after 15 cycles of use, possibly due to partial leaching of gold nanoparticles during catalyst use cycles. The results obtained in this research are certainly relevant and open many possibilities regarding the potential use and scaling of these heterostructures in the photocatalytic production of H₂ from water.

Keywords: hydrogen production; TiO₂; gold nanoparticles; MoS₂; CeO₂; water splitting



Citation: Fontánez, K.; García, D.; Ortiz, D.; Sampayo, P.; Hernández, L.; Cotto, M.; Ducongé, J.; Díaz, F.; Morant, C.; Petrescu, F.; et al. Biomimetic Catalysts Based on Au@TiO₂-MoS₂-CeO₂ Composites for the Production of Hydrogen by Water Splitting. *Int. J. Mol. Sci.* **2023**, *24*, 363. <https://doi.org/10.3390/ijms24010363>

Academic Editor: Shaodong Zhou

Received: 27 November 2022

Revised: 16 December 2022

Accepted: 22 December 2022

Published: 26 December 2022



Copyright: © 2022 by the authors. Licensee MDPI, Basel, Switzerland. This article is an open access article distributed under the terms and conditions of the Creative Commons Attribution (CC BY) license (<https://creativecommons.org/licenses/by/4.0/>).

1. Introduction

There is a global concern about the present and future consequences of climate change. One of the main focuses in the last decade has been cutting or reducing the dependence of fossil fuels to meet our energy requirements [1,2]. Hydrogen, as an energy vector [3], is a promising candidate because it can be obtained from renewable sources like water, its combustion products are mainly water or water vapor, is less toxic than gasoline or any other usual fuel, among others [4,5].

Photosynthesis is considered the best and most efficient model that allows the conversion of solar energy for the generation of clean fuel. In nature, photosynthesis operates by supplying electrons to the active center of photosystem-II. This process is carried out through four consecutive steps of proton-coupled electron transfer, generating, as a final

result of the process, products derived from reduced carbon that are the basis of life and biological activity. Considering the inspiration of this natural process, continuous efforts have been made for decades to implement and assemble some of these photosynthetic mechanisms in order to use solar energy to generate oxygen and hydrogen by splitting water [6–8].

One of the methods to produce hydrogen via water splitting is by photocatalysis [9–11]. Usually semiconductors including titanium oxide (TiO_2), zinc oxide (ZnO), iron (III) oxide (Fe_2O_3), zinc sulfide (ZnS), zirconium oxide (ZrO_2), cadmium sulfide (CdS), among others, are selected as photocatalysts due to their narrow bandgap and electronic structure [12–15]. TiO_2 is one of the most studied and used catalysts in photocatalysis for the reduction of water and degradation of organic pollutants [16], although it presents some disadvantages: (1) Recombination of photo-generated electron hole pairs [17]; (2) Fast backward reaction [18]; and (3) Inability to use visible light. The band gap of TiO_2 is 3.2 eV for anatase, 3.0 eV for rutile, and 3.4 eV for brookite, and with this band gap energy, only ultraviolet light (UV) can be used for hydrogen production [19]. To work with these limitations, multiple chemical modifications have been developed and implemented over the years.

One of them is the incorporation of noble metals, such as silver (Ag), gold (Au) and platinum (Pt), on the surface of titanium oxide due to the ability of the noble metal nanoparticles in reducing the fast recombination of the photogenerated charge carriers, enabling the use of visible light [20]. By reducing the photogenerated charge carriers, the UV activity is increased due to the electron transfer from the CB of TiO_2 to the noble metal nanoparticles [21]. The photoactivity in the visible range of the electromagnetic spectrum can be explained due to the surface plasmon resonance effect and charge separation by the transfer of photoexcited electrons from the metal nanoparticles to the CB of TiO_2 [22]. Obtaining heterostructures by coupling two or more materials with different properties makes it possible to improve the photocatalytic activity of the system [23,24]. Among these heterostructures, it is worth highlighting TiO_2 - ZnO , TiO_2 - WO_3 , TiO_2 - CdS , TiO_2 - SO_2 , among others, which have shown considerable improvements compared to the materials used separately [23,24]. A semiconductor that has gained popularity in recent years has been cerium (IV) oxide, CeO_2 . As with TiO_2 , CeO_2 has a high bandgap energy (from 2.6 eV to 3.4 eV, depending on the synthesis process and the material obtained), and high thermal stability. CeO_2 can be synthesized with different morphologies, it can be doped with metal or non-metal ions, it can be combined with other materials to form more efficient heterostructures, and it can be used for a wide variety of catalytic processes [25]. The incorporation of metal dichalcogenides, such as molybdenum disulfide (MoS_2), has also been explored to replace the use of noble metal co-catalysts due to its high abundance, low cost, good stability, and high catalytic activity [26]. However, the use of MoS_2 could also reduce the charge transfer rate and, therefore, the efficiency in some catalytic hydrogen production processes [27].

As shown above, there is no perfect catalyst to produce hydrogen by water splitting. Therefore, the objective of this research has been to explore the capabilities of different materials to produce hydrogen under visible and ultraviolet light and to combine these to obtain catalytically active heterostructures. To achieve this, different cocatalysts were incorporated onto TiO_2 . The fifteen photocatalysts synthesized are made up of gold nanoparticles (Au NPs; 1%, 3%, 5% by weight), cerium (IV) oxide nanoparticles (CeO_2 NPs; 1%, 3%, 5% by weight), and molybdenum disulfide (MoS_2 ; 1%, 3%, 5% by weight), and have been fully characterized and evaluated in the photocatalytic reaction of hydrogen production by water splitting.

2. Results and Discussion

2.1. Characterization of Catalysts

Fifteen catalysts were synthesized, based on Au nanoparticles deposited on TiO_2 nanowires (TiO_2 NWs), MoS_2 , and CeO_2 nanoparticles (CeO_2 NPs). The proportion of Au nanoparticles, as well as MoS_2 and CeO_2 NPs, were conveniently varied, consider-

ing TiO₂NWs as the base component. These catalysts were used for the hydrogen evolution reaction (HER) from the photocatalytic decomposition of water, and the most efficient catalyst (3%Au@TiO₂NWs-5%MoS₂-5%CeO₂NPs) was fully characterized by different techniques.

Table S1 shows the BET surface area of the different components and of the synthesized catalysts. As can be seen, TiO₂NWs shows a high surface area of 236 m²/g that increases with the incorporation of Au nanoparticles on the surface, going from 242 m²/g (1%Au@TiO₂NWs) to 263 m²/g (3%Au@TiO₂NWs), and to 275 m²/g (5%Au@TiO₂NWs). This effect of increasing the area by incorporating nanoparticles has been previously described [28]. The other two components of the synthesized catalysts (MoS₂ and CeO₂NPs) also show high areas that justify the high area values observed in the catalysts, which range between 248 and 396 m²/g. As can be seen in Table S1, in general, the surface area increases with the addition of Au, although this trend is not so clear with the increase of the other two components.

The catalyst precursors were characterized by electron microscopy. Figure 1a shows the HR-SEM image of TiO₂NWs, characterized by being formed by square-section wires, with diameters ranging from ca. 200 to 300 nm and lengths of up to 10 µm. MoS₂, previously delaminated by prolonged ultrasound treatment, shows a layered structure with variable lengths from 1 to 2 µm (see Figure 1b). The effect of exfoliation of MoS₂, by high power ultrasound, can be seen in the HR-SEM micrograph of Figure S1, taken at low magnification. Figure S1 shows a MoS₂ particle in an intermediate stage of delamination, and before the layers have dispersed. CeO₂NPs are characterized by presenting spherical aggregates of more than 400 nm which, in turn, are formed by very homogeneous nanoparticles with sizes ranging from 4 to 6 nm (Figure 1c). Figure 1d shows the HR-SEM image of the catalyst that showed the highest efficiency (3%Au@TiO₂NWs-5%MoS₂-5%CeO₂NPs). As can be seen in Figure 1d, the different components of the catalyst show a good dispersion. The components of the studied catalysts were characterized by HR-TEM. Figure 2a shows the atomic resolution image of TiO₂NWs. The material is highly crystalline, showing the distinct lattice fringes with an interplanar spacing of 0.33 nm, indexed to (110) crystal plane which corresponds to the rutile phase [29]. On the other hand, the growth of TiO₂NWs takes place along (001) direction determined by HR-TEM image, which is consistent with XRD results that will be discussed later. MoS₂ shows a high level of exfoliation (Figure 2b), which allows us to observe the detail of the atomic structure of a monolayer. As can be seen in the inset of Figure 2b, corresponding to the selected area electron diffraction (SAED), the material is highly crystalline. Apparently, and although it is still to be confirmed, the HR-TEM analyses seem to indicate the presence of structural defects generated by the appearance of vacancies in the two-dimensional structure of the material. These defects could be due to the intense exfoliation process produced by high intensity ultrasound, and could be related to the high activity of the catalysts. Figure 2c shows the HR-TEM image of CeO₂NPs. As seen in the SAED, the material is crystalline. Part of the image has been further magnified to show detail of the lattice fringes, with an interplanar spacing of 0.31 nm, indexed to (111) crystal plane corresponding to the characteristic face-centered cubic fluorite-type structure [30].

Figure 3 shows the results obtained by X-ray diffraction (XRD) for the most efficient catalyst (3%Au@TiO₂NWs-5%MoS₂-5%CeO₂NPs), along with that of MoS₂, CeO₂NPs and TiO₂NWs for comparison purposes. As shown in Figure 3a, well-defined diffraction peaks are observed at ca. 14°, 32°, 39°, 49°, and 59° that have been ascribed to (002), (100), (103), (105), and (110) planes of 2H-type MoS₂ hexagonal phase (JCPDS # 75-1539), respectively [31–33]. Figure 3b shows the diffraction pattern of CeO₂NPs. The most intense peaks are observed at ca. 28°, 33°, 47° and 56°, and correspond to (111), (200), (220) and (311) crystal planes, respectively [34–36]. These peaks are characteristic of CeO₂ with face-centered cubic fluorite-type structure. Figure 3c shows the XRD pattern of TiO₂NWs. The diffraction peaks at ca. 27°, 36°, 41°, y 54° were ascribed to (110), (101), (111), y (211) TiO₂ crystalline planes in rutile phase (JCPDS 75-1750) [37,38]. The XRD of the most efficient

catalyst is shown in Figure 3d. As can be seen there, the main peaks of all three components are present. However, the presence of Au, which should be shown as a very low intensity peak at ca. 38° [39], corresponding to Au (111), is not observed in the catalyst, possibly due to the high dispersion of the metal.

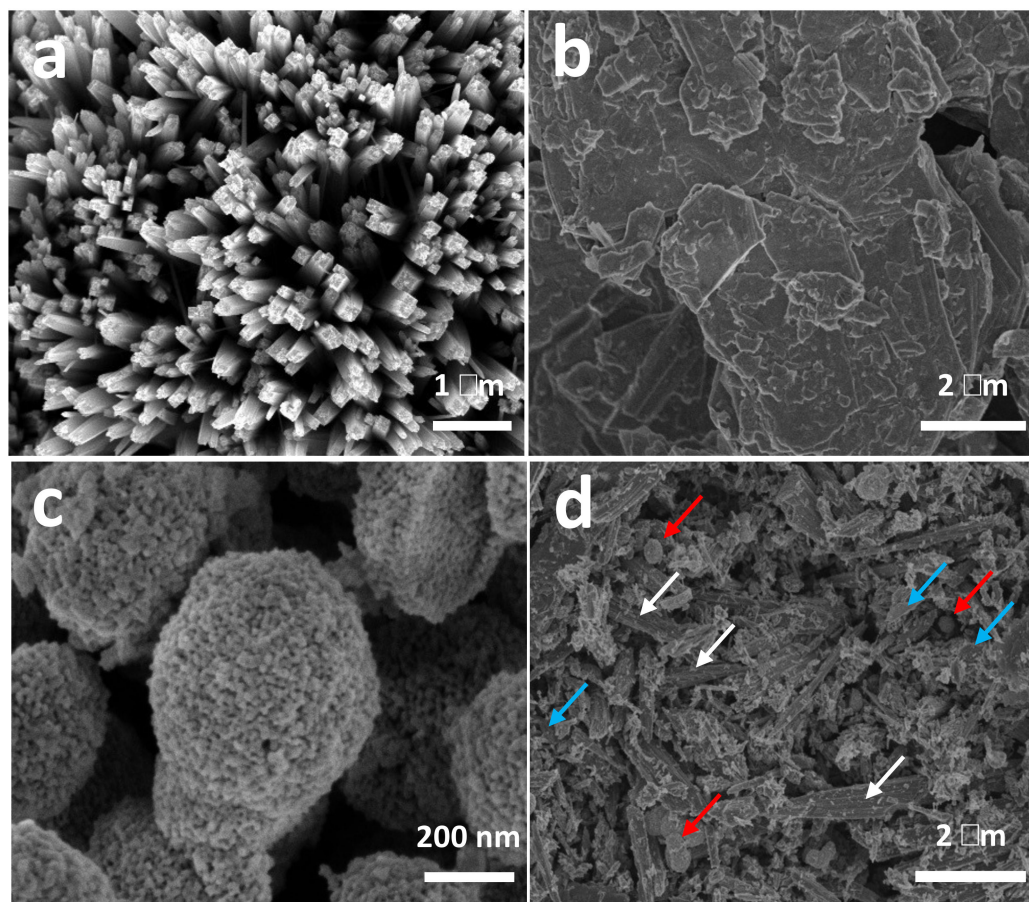


Figure 1. HR-SEM micrographs of TiO_2NWs (a), MoS_2 nanosheets (b), CeO_2NPs (c) and the 3%Au@ TiO_2NWs -5% MoS_2 -5% CeO_2NPs catalyst (d). The arrows in (d) indicate the different components of the catalyst: TiO_2NWs (white), MoS_2 (blue), and CeO_2NPs (red).

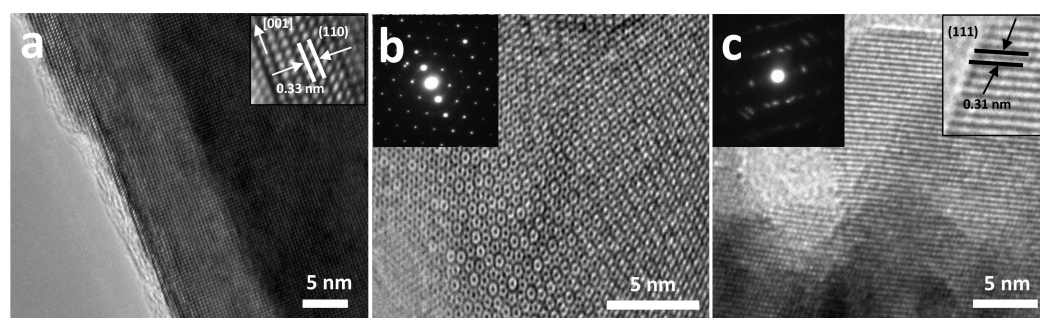


Figure 2. HR-TEM micrographs of the different components of the catalysts: TiO_2NWs and inset at atomic resolution showing the direction of growth and the lattice fringes (a); MoS_2 single layer and inset corresponding to the selected area electron diffraction, SAED (b); and CeO_2NPs and insets corresponding to SAED and micrograph at higher magnification showing the lattice fringes (c).

The different materials, as well as the most efficient catalyst, were characterized by Raman spectroscopy (Figure 4). MoS_2 shows two very characteristic bands at 383 cm^{-1} and 407 cm^{-1} (Figure 4a), which have been assigned to the E_{2g}^1 and A_{1g} modes, respectively [40].

The position of these bands has been correlated with the number of layers of the material, so the results suggest that the exfoliation process was very efficient, generating MoS₂ flakes with few layers [41,42]. CeO₂NPs (Figure 4b) shows an intense band at ca. 457 cm⁻¹, and a much less pronounced one at 607 cm⁻¹ that have been assigned to a cubic fluorite structure, as already evidenced from the XRD results. The main band at 457 cm⁻¹ corresponds to a triply degenerate F_{2g} mode of symmetric stretching vibrations of oxygen ions around Ce⁴⁺ ions in octahedral CeO₈ [43]. The asymmetry of the band at 457 cm⁻¹ has been associated with structural defects due to the presence of oxygen vacancies in the oxide [44,45], which could also be correlated with the reactivity of the material. Figure 4c shows the Raman spectrum of TiO₂NWs, whose bands at ca. 448 cm⁻¹ and 610 cm⁻¹ have been assigned to the vibration modes E_g and A_{1g} of TiO₂ in the rutile phase, as already evidenced by XRD. The Raman spectrum of the most efficient catalyst (Figure 4d) shows two pronounced bands at 448 cm⁻¹ and 610 cm⁻¹, and a shoulder at ca. 687 cm⁻¹. These three bands come from rutile, which is the major component of the catalyst. Additionally, two small peaks are observed at ca. 384 cm⁻¹ and 407 cm⁻¹ assigned to MoS₂. Due to the position of the CeO₂NPs bands, the signal of this material is masked under the strong contribution of rutile.

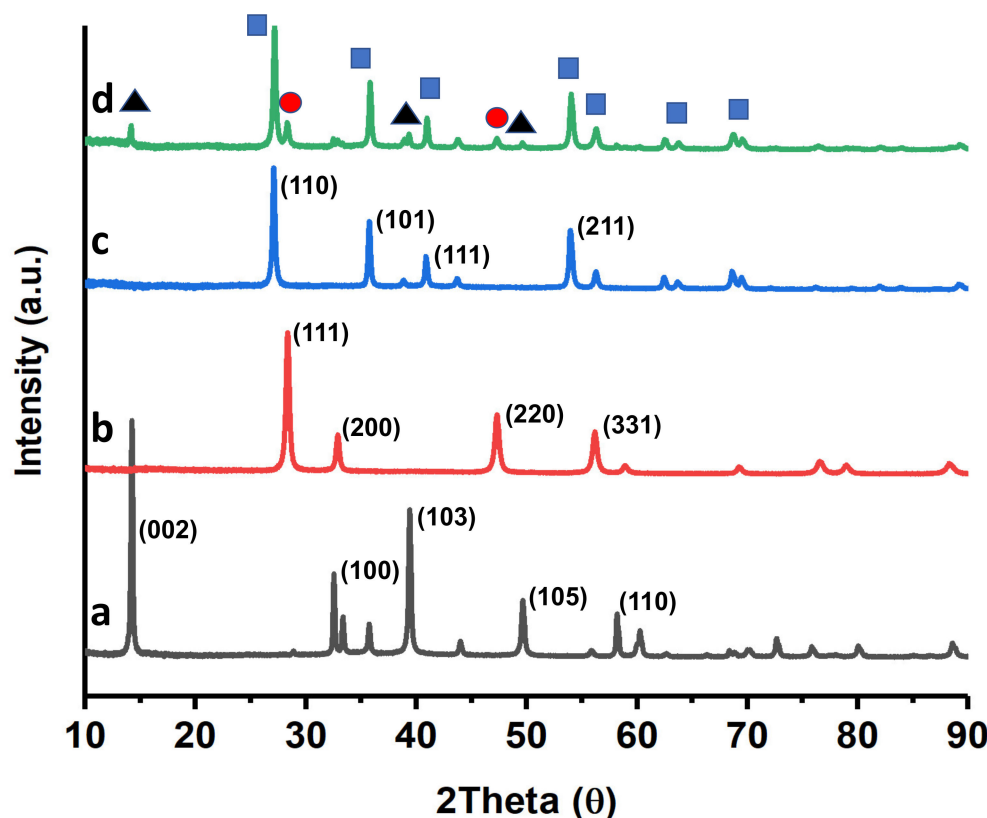


Figure 3. XRD patterns of MoS₂ (a); CeO₂NPs (b); TiO₂NWs (c); and 3%Au@TiO₂NWs-5%MoS₂-5%CeO₂NPs (d). The most intense peaks in the catalyst have been associated with the different components (black triangles: MoS₂, red circles: CeO₂NPs, blue squares: TiO₂NWs).

The most efficient catalyst (3%Au@TiO₂NWs-5%MoS₂-5%CeO₂NPs) was also characterized by X-ray photoelectron spectroscopy (XPS). Ti2p (Figure 5a) shows two components at 464.3 eV and 458.7 eV that were ascribed to the Ti2p_{1/2} and Ti2p_{3/2} transitions, respectively [3,9]. These transitions are quite symmetrical, so any additional contribution was ruled out. Figure 5b shows the transition corresponding to O1s. As can be seen, the transition is clearly asymmetric and has been deconvoluted into two components at ca. 530.3 eV and 532.3 eV. The most intense peak (530.3 eV) has been assigned to oxygen in the TiO₂ lattice [3,46], which also masks the possible contribution of oxygen in the CeO₂ lattice, while

the component observed at 532.3 eV has been assigned to oxygen vacancies in CeO₂ [47] (as suggested by the asymmetry of the main peak of CeO₂NPs in Raman spectroscopy), or to non-lattice oxygen [46]. Figure 5c shows the Au4f transition, with peaks at 84.1 eV and 87.7 eV and a characteristic spin-orbit splitting of ca. 3.6 eV, which have been clearly assigned to the presence of metallic Au [48]. The transition corresponding to Ce3d is shown in Figure 5d. This transition, which is very complex due to a state hybridization process, evidences two distinguishable series of peaks corresponding to the Ce⁴⁺ and Ce³⁺ species. The different peaks were labeled u, u', u'', v, v' and v'' to represent the different electronic states of Ce⁴⁺ and Ce³⁺ [47,49]. The presence of Ce³⁺ ions gives rise to a charge imbalance, responsible for oxygen vacancies and the presence of defects and unsaturated chemical bonds in the nanomaterial. These defects in CeO₂NPs support the results previously shown by Raman and XPS.

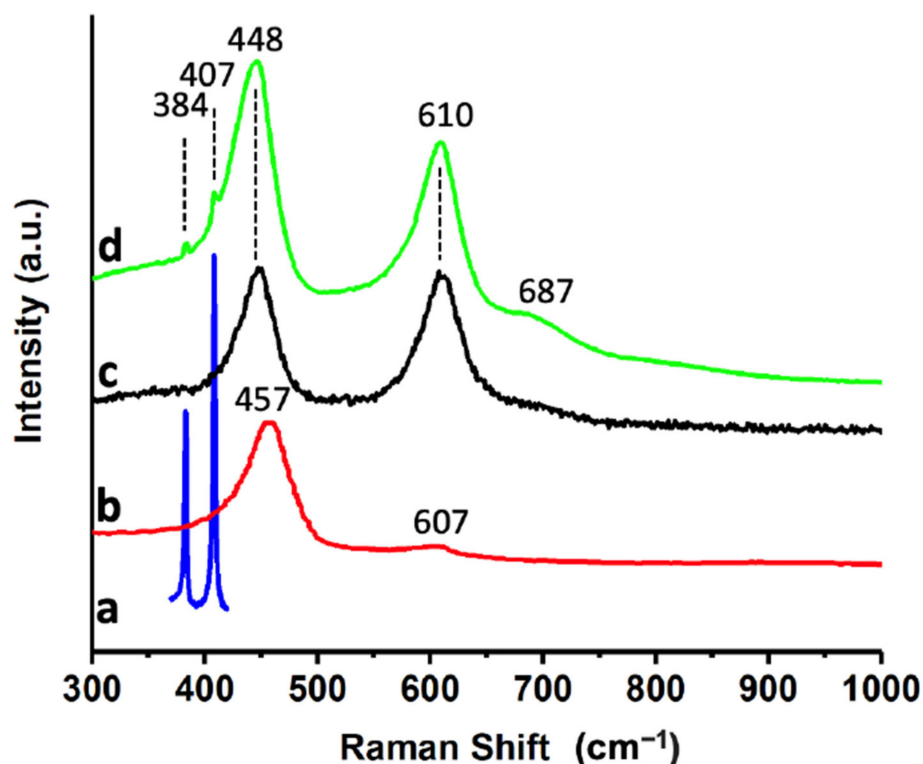


Figure 4. Raman spectra of MoS₂ (a); CeO₂NPs (b); TiO₂NWs (c); and 3%Au@TiO₂NWs-5%MoS₂-5%CeO₂NPs (d).

Figure 5d shows the Mo3d and S2s transitions. The Mo3d shows two peaks at 232.4 eV and 229.2 eV, which have been attributed to the Mo3d_{3/2} and Mo3d_{5/2} doublet, respectively, characteristic of the Mo⁴⁺ state in MoS₂ [48,50]. The observed peak at ca. 226.4 eV was assigned to S2s [48], typical of MoS₂. The slight asymmetry of the Mo3d peaks could point to a possible mixture of oxidation states, which could also be correlated with the potential presence of defects in the material lattice and reactivity.

The efficiency of radiation absorption by the catalysts is a critical factor for their activity, so the different catalysts and nanomaterials used were analyzed using Tauc diagrams [51]. As shown in Figure 6, TiO₂NWs showed a bandgap in the border region between UV and visible (2.95 eV), slightly different from the expected value for TiO₂ in rutile phase (3.05 eV) [52]. CeO₂NPs and MoS₂ show bandgaps at 2.61 eV and 2.46 eV, respectively, clearly in the visible region. The most efficient catalyst, formed as a heterostructure of these components in addition to the presence of Au nanoparticles, shows a bandgap at 2.23 eV (ca. 555 nm), which clearly justifies the activity of the 3%Au@TiO₂NWs-5%MoS₂-5%CeO₂NPs

heterostructure under irradiation with visible light, as will be described in the section corresponding to catalytic results.

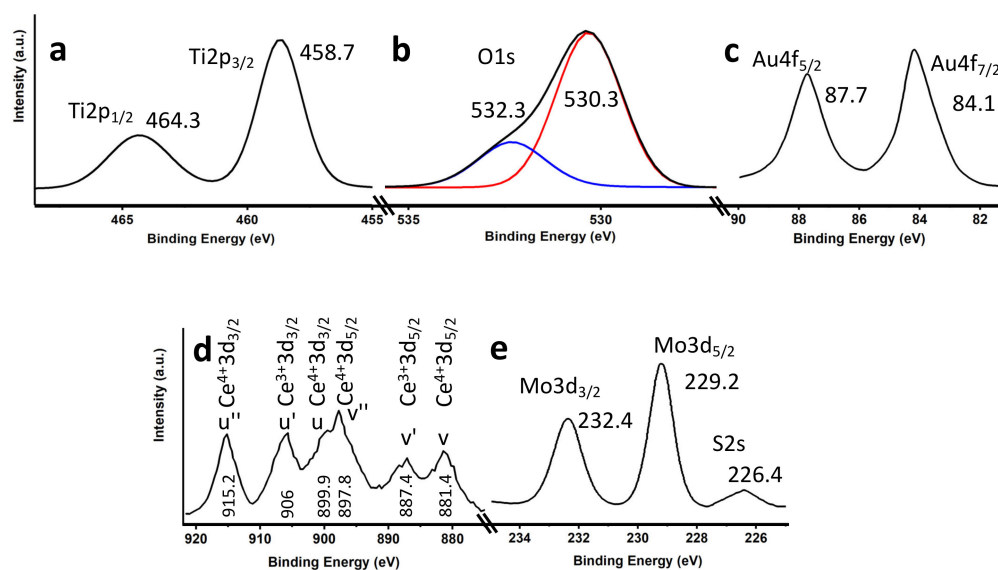


Figure 5. XPS core level spectra for Ti2p (a); O1s (b); Au4f (c); Ce3d (d); and Mo3d/S2s (e).

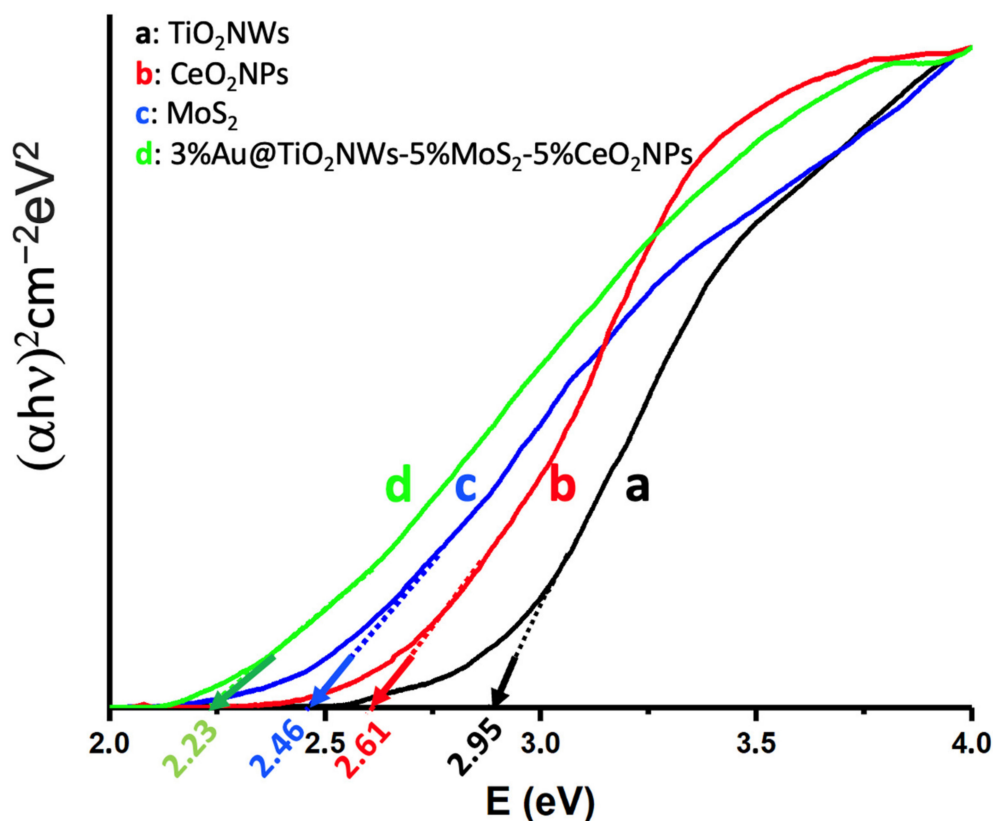


Figure 6. Tauc plots of $(\alpha h\nu)^2$ versus energy (eV), and determination of the bandgap energy of TiO₂NWs (a); CeO₂NPs (b); MoS₂ (c); and 3%Au@TiO₂NWs-5%MoS₂-5%CeO₂NPs (d).

2.2. Photocatalytic Hydrogen Production

Before proceeding to evaluate the activity of the synthesized catalysts, several preliminary studies were carried out to establish the optimal reaction conditions. To do this, we started from the heterostructure with the highest proportion of each of the components

(5%Au@TiO₂NWs-5%MoS₂-5%CeO₂NPs). Initially, a study of the optimum pH was carried out (see Figure S2a), and it was established that the most suitable was pH = 7. Another of the preliminary studies that was carried out allowed establishing the optimum amount of catalyst in the reaction medium. As can be seen in Figure S2b, there is a clear correlation between the amount of catalyst and the HER efficiency, so a loading of 50 mg of catalyst (for a total reaction volume of 100 mL) was established as the optimal amount.

The photocatalytic efficiency of the catalysts for the evolution of H₂ was evaluated in the presence of Na₂SO₃ (0.02 M) and Na₂S (0.4 M) as sacrificial reagents. In all cases, it was found that there is no evolution of H₂ without either photocatalyst or irradiation (see Figure S2c). Figure 7 shows the results of the photocatalytic hydrogen production from the fifteen synthesized catalysts. In all cases, the activity under irradiation with different wavelengths (220, 280, 320, 400, 500, 600 and 700 nm) was evaluated. As can be seen, the maximum hydrogen production is observed under irradiation at 400 nm, this wavelength being the one corresponding to the bandgap of TiO₂NWs (see Table S2). At more energetic wavelengths the behavior varies from one system to another. Figure 7a,d, corresponding to the heterostructures Au@TiO₂NWs-5%MoS₂-3%CeO₂NPs and Au@TiO₂NWs-5%MoS₂-1%CeO₂NPs, respectively, show a similar trend under irradiation at 220, 280 and 320 nm, with stable values of hydrogen production in catalysts with 3% and 5% Au. Catalysts with lower Au loading (1%) show much lower activities. In all the catalysts a decrease in activity is observed under irradiation in the visible range ($\lambda > 400$ nm), although surprisingly hydrogen production is observed even at very low energy wavelengths (i.e., 700 nm). This behavior clearly points to a synergy between the different nanomaterials, and specifically to the gold load, which, as observed, has a significant effect on the levels of hydrogen production. The highest catalytic activity is observed with 3%Au@TiO₂NWs-5%MoS₂-5%CeO₂NPs, showing a hydrogen production of 1114 $\mu\text{m}/\text{hg}$ under irradiation at 400 nm. In contrast, the catalyst with the lowest efficiency was the Au@TiO₂NWs-5%MoS₂-1%CeO₂NPs heterostructure, and specifically the one with 1%Au, with only a hydrogen production of 606 $\mu\text{m}/\text{hg}$ (Figure 7d). This behavior is evidence of the relevance of CeO₂NPs in the heterostructure. As previously discussed in Section 2.1, CeO₂NPs present oxygen vacancies and defects that may be responsible for the reactivity of the material. These defects, as already described [47], might originate from the effective separation of photogenerated electron-hole pairs within the composite endorsing the charge transfer efficiency. The effect of MoS₂ on the catalyst activity is indisputable, although it is not as relevant as for CeO₂NPs. When comparing the catalysts Au@TiO₂NWs-1%MoS₂-5%CeO₂NPs (Figure 7e), Au@TiO₂NWs-3%MoS₂-5%CeO₂NPs (Figure 7b) and Au@TiO₂NWs-5%MoS₂-5%CeO₂NPs (Figure 7c) it is observed that by increasing the amount of MoS₂ the production of H₂ also increases substantially. This effect is more notable when going from 3% to 5% of MoS₂ in the heterostructure. MoS₂ has high surface area values, as shown in Table S1. The increase in MoS₂ loading produces an increase in the specific area of the heterostructure, together with the improvement in the conductivity properties of the catalyst [53], which could justify the effect of this nanomaterial on the reactivity observed in Figure 7. On the other hand, the presence of Au, and especially the generation of surface plasmons generated by the Au nanoparticles on the surface of the heterostructure [54], represents an adjuvant factor on the photocatalytic HER.

The recyclability of the most efficient catalyst (3%Au@TiO₂NWs-5%MoS₂-5%CeO₂NPs) was also evaluated. For this, 15 consecutive reactions were carried out with the same catalyst (Figure S3) using a larger reaction volume (200 mL). After each reaction, the catalyst was recovered by centrifugation (3000 rpm, 15 min), washed with deionized water, and dried overnight in an oven at 50 °C. The recovered catalyst was used again in the next reaction, using the same experimental conditions, and keeping the reaction temperature constant at 20 °C. After 15 cycles of use, the results obtained (Figure S3) showed an efficiency of ca. 93% of the initial, which represents a loss of activity of around 7%. After cycle 15, the catalyst showed similar morphological characteristics although, according to EDX measurements, the gold loading was slightly reduced to approximately 2.4%, which could

indicate a gold leaching effect during the use cycles, that would justify the loss of 7% of activity. This result is remarkable considering that the catalysts are heterostructures formed by four components whose synergistic behavior remains almost unchanged in each cycle of use.

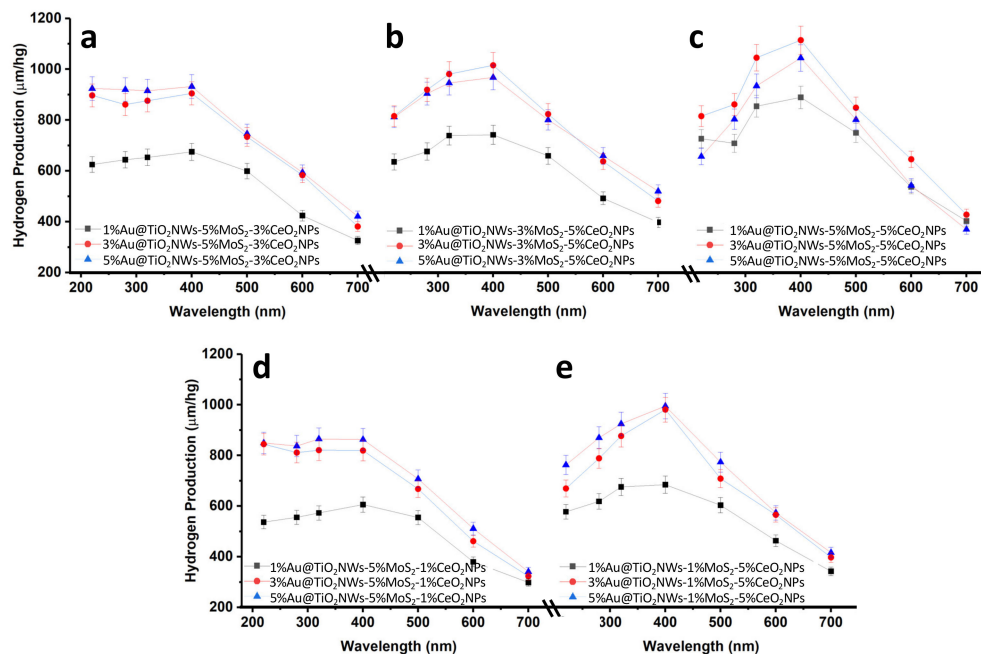


Figure 7. H₂ production profiles of the synthesized catalysts under irradiation at different wavelengths (the legends corresponding to the catalysts are shown in each of the figures). The estimated error bars for each of the values obtained are also shown.

Some results of recent studies on hydrogen production by water splitting using heterostructured catalysts are shown in Table S3 [55–62]. As can be seen there, the amount of hydrogen reported in our research is one of the highest, although a direct comparison with other research is not possible because the experimental conditions, reaction time, and even nanomaterials are not the same. Nonetheless, our hydrogen production results are certainly promising, and could potentially even be applicable to larger-scale processes.

2.3. Mechanism of the Photocatalytic Hydrogen Production

Figure S4 shows the effect of incorporating hole scavengers (methanol and EDTA-Na₂) on HER. Figure S4a to Figure S4e show the most efficient systems in the absence of scavengers and in the presence of each of them. As can be seen, the addition of methanol (5 mL) to the reaction medium clearly increases the production of hydrogen at all wavelengths. The effect of the addition of EDTA-Na₂ (0.1 M) produces an even greater effect, with pronounced increases in all the systems used and practically under any irradiation energy. The incorporation of larger amounts of methanol or EDTA-Na₂ did not produce significant changes, therefore, at least for these hole scavengers and for the reaction conditions used, the maximum possible H₂ production was reached. These results clearly suggest that electron-hole recombination occurs in the absence of scavengers, despite the effect of electron channeling towards the Au nanoparticles and MoS₂ nanosheets from the catalysts and the use of electron donors (Na₂SO₃, 0.02 M and Na₂S, 0.4 M) in the reaction mixture.

Considering these results, in addition to the determination of bandgaps (see Figure 6), a tentative mechanism for HER has been proposed (Figure 8). To do this, Mulliken's classical theory of electronegativity has been used [63,64], which makes it possible to establish the position of the edge of the band of the different nanomaterials that form the heterostructure and, based on it, to establish the direction of migration of the photogenerated charge carriers in the catalyst (see Equations (1) and (2)).

$$E_{CB} = \chi - E_C - 0.5E_g \quad (1)$$

$$E_{VB} = E_{CB} + E_g \quad (2)$$

where E_{CB} and E_{VB} are the edge potentials of the valence band and the conduction band, respectively, χ is the absolute electronegativity, E_C is the energy of free electrons on the hydrogen scale (4.50 eV) [65,66], and E_g is the experimentally determined bandgap (see Figure 6). The χ values for TiO_2 (rutile) and CeO_2 are 5.81 and 5.56 eV, respectively [67,68]. The E_{CB} and E_{VB} edge positions for TiO_2NWs determined from Equations (1) and (2) are -0.165 and 2.785 eV, respectively, while for CeO_2NPs the calculated values were -0.245 and 2.365 eV (see Figure 8).

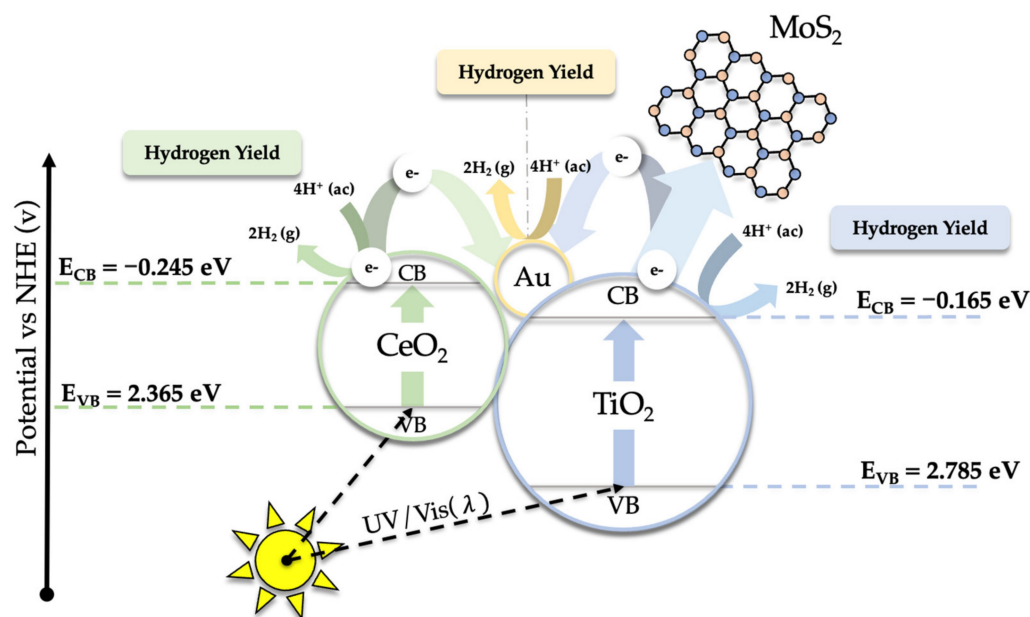


Figure 8. Mechanism proposed for the hydrogen production using $\text{Au@TiO}_2\text{NWs-MoS}_2\text{-CeO}_2\text{NPs}$ catalysts under UV-visible irradiation.

As previously shown [58], the presence of CeO_2NPs and MoS_2 significantly broadens the range of light absorption, which increases the density of photogenerated electrons and the production of H_2 . Under irradiation, the valence band electrons of both TiO_2NWs and CeO_2NPs are photoexcited to their corresponding conduction bands [9]. These electrons can reduce the water, generating H_2 , or be transferred to the MoS_2 or Au nanoparticles. Both MoS_2 and Au act as sinks that channel electrons, prevent electron-hole recombination, and facilitate subsequent reactivity [3,11,69]. The holes that were created in the valence band of the heterostructure, as previously shown, undergo partial recombination with the photogenerated electrons, although this recombination is inhibited by adding hole scavengers (methanol or EDTA-Na_2) to the reaction mixture. As previously described, the presence of Ce^{3+} and Ce^{4+} species, identified by XPS (see Figure 5d), may play a relevant role in prolonging the lifetime of photoinduced charge carriers [58]. Ce^{4+} species can trap the electrons helping to avoid electron-hole recombination. On the other hand, Ce^{3+} /oxygen vacancies can provide abundant H_2O adsorption sites, which decreases the H_2O adsorption energy, increasing the efficiency of the water splitting reaction.

3. Materials and Methods

3.1. Reagents and Materials

All reagents were used as received without further purification. All solutions were prepared with deionized water (Milli-Q water, Burlington, MA, USA, $18.2 \text{ M}\Omega\text{cm}^{-1}$ at 25°C). TiCl_4 (99.9%) was provided by Fisher Scientific, Cayey, Puerto Rico. $\text{HAuCl}_4 \cdot 3\text{H}_2\text{O}$ (ACS Reagent, St. Louis, MO, USA, 49.0 + % Au basis), MoS_2 (Nanopowder, St. Louis,

MO, USA, 90 nm diameter, 99% trace metals basis), $\text{Ce}(\text{NO}_3)_3 \cdot 6\text{H}_2\text{O}$ (99.99%), Ethanol (200 proof, anhydrous, $\geq 99.5\%$), EDTA disodium salt dihydrate (OmniPur, St. Louis, MO, USA), and NaBH_4 (99.99% trace metals basis) were provided by Sigma Aldrich (Darmstadt, Germany). Methanol anhydrous for UHPLC-MS LiChrosolv (99.9%) was provided by Supelco (Bellefonte, PA, USA). Silicon p-type boron doped substrates (Si <100>), were provided by El-CAT (Ridgefield Park, NJ, USA). UHP N_2 (5.0), used for the photocatalytic reaction, was provided by Praxair, Gurabo, Puerto Rico.

3.2. Synthesis of Nanomaterials

The synthesis of titanium oxide nanowires (TiO_2NWs) has been previously described [70]. In a typical synthesis, a mixture of water and HCl (37% solution) (1:1, *v/v*) was prepared. Subsequently, TiCl_4 (3 mL) was added dropwise to 100 mL of the solution and allowed to mix for 30 min until the presence of suspended particles was not observed. The solution was then transferred to Teflon-lined autoclaves, and silicon substrates (Si <100>) with the polished surface facing the inside of the Teflon container, were incorporated into the solution. The autoclaves were then sealed and transferred to an oven. The autoclaves were treated at 180 °C for 24 h. Once the treatment time had elapsed, the autoclaves were left to cool for at least 12 h. As a result, the growth of a white deposit on the surface of the Si substrates was observed. The material obtained was washed with abundant deionized water, dried in an oven at 60 °C and stored in vials that were sealed until later use.

The deposition of gold nanoparticles (AuNPs) was carried out by dispersing 1 g of the support (TiO_2NWs), whose synthesis was previously described, in 100 mL of H_2O and the mixture was sonicated for 30 min. Next, the required amount of gold precursor ($\text{HAuCl}_4 \cdot 3\text{H}_2\text{O}$) was added to the reaction mixture and stirred for 1 h. Finally, the process continued with the reduction of gold by adding, dropwise, a NaBH_4 solution (10 mg in 10 mL of H_2O) under constant stirring. Once the 10 mL of NaBH_4 had been added, the resulting solution was kept under stirring for 1 h. The reaction product was separated by centrifugation (3000 rpm, 15 min), washed 4 times with deionized water, and dried overnight at 60 °C. The different Au@ TiO_2NWs compounds were synthesized with 1%, 3% and 5% AuNPs on the surface and these materials were later used for the incorporation of the rest of the catalyst components.

CeO_2 nanoparticles (CeO_2NPs) were obtained through a coprecipitation process. For this, two solutions were prepared: (i) 250 mL of a solution of $\text{Ce}(\text{NO}_3)_3 \cdot 6\text{H}_2\text{O}$ (0.02 M) and (ii) 250 mL of a solution of K_2CO_3 (0.03 M). Both solutions were introduced dropwise into an Erlenmeyer flask containing 50 mL of water. During this process, the mixture was kept under constant stirring. As a result, a precipitate of $\text{Ce}_2(\text{CO}_3)_3$ was obtained, which was separated from the solution by centrifugation. The resulting solid was washed four times with deionized water and dried at 70 °C for 3 h. Next, the dry material was calcined in a muffle at 600 °C for 3 h, using an open crucible.

The commercial MoS_2 was subjected to an exfoliation process before being used. For this, 4 g of MoS_2 were mixed with 200 mL of deionized water. The resulting dispersion was sonicated using a Cole-Palmer Tip Sonicator (Cole-Parmer 750-Watt Ultrasonic Processor) for 6 h in pulsed mode (40% amplitude, pulse on 5 s, pulse off 10 s). Subsequently, the solution was kept static for sedimentation for 3 h. Next, the supernatant was extracted from the mixture and centrifuged for 30 min at 3000 rpm to remove the non-delaminated MoS_2 . Next, the supernatant can be dried by evaporation at 50 °C to be used later, or manipulated directly as a suspension. The concentration of the suspension can be determined by measuring the absorbance at 672 nm, using the Beer-Lambert law, and considering ϵ as $3400 \text{ mL mg}^{-1} \text{ m}^{-1}$.

The materials, whose synthesis has been described above, were used for the following stages of preparation of the catalysts. Thus, 300 mg of Au@ TiO_2NWs were dispersed in a solution containing 20 mL of ethanol and 20 mL of deionized water, and the mixture was vigorously stirred for 1 h. Subsequently, cerium oxide nanoparticles (CeO_2NPs) were added, and the suspension was stirred for 2 h. The product was then separated from

solution by centrifugation (3000 rpm, 15 min), washed 4 times with deionized water, and dried overnight at 60 °C. The incorporation of MoS₂ was carried out in a final synthesis step, and by a procedure similar to that previously described for CeO₂NPs. Once the synthesis process was finished, the product was recovered by centrifugation (3000 rpm, 15 min), washed four times with deionized water, dried overnight at 60 °C, and stored and sealed at room temperature until later use. The 15 synthesized catalysts, based on Au@TiO₂NWs-MoS₂-CeO₂NPs, were identified indicating the percentage of gold incorporated on the surface and the percentages of MoS₂ and CeO₂NPs in each case.

3.3. Characterization of the Catalysts

The surface morphology of the catalysts was evaluated using a FEI Verios 460 L High Resolution Scanning Electron Microscope (HR-SEM, Thermo Fisher Scientific, Hillsboro, OR, USA), equipped with a Quantax EDS Analyzer, and by High Resolution Transmission Electron Microscopy (HR-TEM), using a JEOL JEM 3000F (300 kV) microscope. XPS measurements were carried out using an ESCALAB 220i-XL spectrometer, using non-monochromatic Mg K α (1253.6 eV) radiation from a twin anode, operating at 20 mA and 12 kV in the constant analyzer energy mode, with a PE of 50 eV. The crystallinity of the catalysts was studied by X-ray diffraction, using a Bruker D8-Advance diffractometer that operates at 40 kV and 40 mA in the range of 20–80°, using a Bragg-Brentano configuration, and at a scan speed of 1° min^{−1}. The catalysts were also characterized by Raman spectroscopy, using a DXR Thermo Raman Microscope, which uses a 532 nm laser source at 5 mW power and a 25 μ m pinhole aperture with a 5 cm^{−1} nominal resolution. Bandgap measurements of the different materials were carried out using a Perkin Elmer Lambda 365 UV-Vis spectrophotometer (Perkin Elmer, Waltham, MA, USA), equipped with an integrating sphere. The bandgap value was obtained from the graph of the Kubelka-Munk function versus the absorbed light energy [51]. Brunauer Emmett Teller (BET) specific area measurements were carried out using a Micromeritics ASAP 2020 system, according to N₂ adsorption isotherms at 77 K.

3.4. Photocatalytic Hydrogen Production

The experimental setup for the characterization of the catalysts for the hydrogen evolution reaction (HER) by photocatalytic water splitting consisted of mixing 50 mg of the desired catalyst with 100 mL of deionized water in a 200 mL quartz reactor. Next, sacrificial electron donor solutions (Na₂SO₃, 0.02 M; Na₂S, 0.4 M) were added. In order to test the effect of adding additional hole scavengers to the reaction mixture, methanol (5 mL) and EDTA-Na₂ (0.1 M) were used. The reaction mixture was kept at 20 °C for 1 h before the start of the reaction, to guarantee temperature stability, and was purged with nitrogen (N₂, 5.0) during the pre-reaction process. Next, the reaction mixture was irradiated using a solar simulator, whose irradiation power in the absence of filters is 120 mW.cm^{−2}). To study the influence of irradiation energy on the water splitting reaction, different cut-off filters at 220, 280, 320, 400, 500, 600, and 700 nm were used, and the reaction was followed for two hours. The hydrogen produced was quantified using a gas chromatograph coupled to a thermal conductivity detector (GC-TCD, Perkin-Elmer Clarus 600).

4. Conclusions

A total of 15 catalysts with different amounts of Au, MoS₂, and CeO₂ (1%, 3%, and 5% by weight) incorporated onto TiO₂NWs were synthesized, and their photocatalytic activity was evaluated by the production of hydrogen via water splitting using visible and ultraviolet light. The highest hydrogen production was 1114 μ m/hg, and was obtained with the 3%Au@TiO₂NWs-5%MoS₂-5%CeO₂NPs composite. The combination of the different materials caused a synergistic effect, increasing the catalytic activity and allowing the use of wavelengths ranging from 220 to the visible range, with remarkable efficiency even under irradiation at wavelengths as low in energy as 700 nm. The recyclability test showed an

efficiency loss of ca. 7% after 15 cycles, suggesting a stable and suitable catalyst for the photocatalytic production of hydrogen by water splitting.

The results obtained in this research are certainly the starting point for further developments that allow us to delve into the mechanisms that control the HER. In this sense, the continuation of this research, already in progress, will analyze three factors that, in our opinion, are of great relevance for the catalytic systems studied: (i) the effect of increasing the loading of MoS₂ and CeO₂NPs in the heterostructure, plus beyond the 5% considered in the present investigation; (ii) analysis of how the use of cerium oxides in which the Ce³⁺/Ce⁴⁺ ratio can be modulated influences HER; and (iii) characterization of possible leaching during catalyst use and regeneration cycles.

Supplementary Materials: The following supporting information can be downloaded at: <https://www.mdpi.com/article/10.3390/ijms24010363/s1>.

Author Contributions: Conceptualization, F.M., C.M. and A.M.; methodology, F.M.; formal analysis, A.M. and F.M.; investigation, K.F., D.G., D.O., P.S., F.D., L.H., C.M. and F.M.; resources, F.M., C.M. and F.P.; writing—original draft preparation, A.M. and F.M.; writing—review and editing, A.M., F.M., C.M., J.D. and M.C.; supervision, A.M. and F.M.; project administration, A.M., F.M. and M.C.; funding acquisition, F.M., A.M., C.M., M.C. and J.D. All authors have read and agreed to the published version of the manuscript.

Funding: Financial support from NSF Center for the Advancement of Wearable Technologies-CAWT (Grant 1849243), from the Consortium of Hybrid Resilient Energy Systems CHRES (DE-NA0003982), from The Puerto Rico-Louis Stokes Alliance for Minority Participation, PR-LSAMP (HRD-2008186), and from the Spanish Ministry of Economy and Competitiveness, under NanoCat-Com Project (PID2021-124667OB-I00), are gratefully acknowledged.

Institutional Review Board Statement: Not applicable for studies not involving humans or animals.

Informed Consent Statement: Not applicable.

Data Availability Statement: The data is contained in the article and is available from the corresponding authors on reasonable request.

Acknowledgments: The facilities provided by the National Center for Electron Microscopy at Complutense University of Madrid (Spain), by “Instituto de Micro y Nanotecnología IMN-CNM, CSIC, CEI UAM + CSIC” and by the Materials Characterization Center at University of Puerto Rico are gratefully acknowledged. K.F. thanks PR NASA Space Grant Consortium for a graduate fellowship (#80NSSC20M0052). D.O. thanks Consortium of Hybrid Resilient Energy Systems (CHRES) for a graduate fellowship. L.H. thanks PR-LSAMP for an undergraduate fellowship (HRD-2008186).

Conflicts of Interest: The authors declare no conflict of interest.

References

1. Gustavsson, L.; Nguyen, T.; Sathre, R.; Tetley, U.Y.A. Climate Effects of Forestry and Substitution of Concrete Buildings and Fossil Energy. *Renew. Sustain. Energy Rev.* **2021**, *136*, 110435. [CrossRef]
2. Hassan, A.; Ilyas, S.Z.; Jalil, A.; Ullah, Z. Monetization of the Environmental Damage Caused by Fossil Fuels. *Environ. Sci. Pollut. Res.* **2021**, *28*, 21204–21211. [CrossRef] [PubMed]
3. Machín, A.; Cotto, M.; Ducongé, J.; Arango, J.C.; Morant, C.; Márquez, F. Synthesis and Characterization of Au@TiO₂ NWs and Their Catalytic Activity by Water Splitting: A Comparative Study with Degussa P25. *Am. J. Eng. Appl. Sci.* **2017**, *10*, 298–311. [CrossRef]
4. Atilhan, S.; Park, S.; El-Halwagi, M.M.; Atilhan, M.; Moore, M.; Nielsen, R.B. Green Hydrogen as an Alternative Fuel for the Shipping Industry. *Curr. Opin. Chem. Eng.* **2021**, *31*, 100668. [CrossRef]
5. Qazi, U.Y. Future of Hydrogen as an Alternative Fuel for Next-Generation Industrial Applications; Challenges and Expected Opportunities. *Energies* **2022**, *15*, 4741. [CrossRef]
6. Valdés, Á.; Qu, Z.-W.; Kroes, G.-J.; Rossmesl, J.; Nørskov, J.K. Oxidation and Photo-Oxidation of Water on TiO₂ Surface. *J. Phys. Chem. C* **2008**, *112*, 9872–9879. [CrossRef]
7. Schley, N.D.; Blakemore, J.D.; Subbaiyan, N.K.; Incarvito, C.D.; D’Souza, F.; Crabtree, R.H.; Brudvig, G.W. Distinguishing Homogeneous from Heterogeneous Catalysis in Electrode-Driven Water Oxidation with Molecular Iridium Complexes. *J. Am. Chem. Soc.* **2011**, *133*, 10473–10481. [CrossRef]

8. Etacheri, V.; Di Valentin, C.; Schneider, J.; Bahnemann, D.; Pillai, S.C. Visible-Light Activation of TiO₂ Photocatalysts: Advances in Theory and Experiments. *J. Photochem. Photobiol. C Photochem. Rev.* **2015**, *25*, 1–29. [\[CrossRef\]](#)
9. Pinilla, S.; Machín, A.; Park, S.-H.; Arango, J.C.; Nicolosi, V.; Márquez-Linares, F.; Morant, C. TiO₂-Based Nanomaterials for the Production of Hydrogen and the Development of Lithium-Ion Batteries. *J. Phys. Chem. B* **2018**, *122*, 972–983. [\[CrossRef\]](#)
10. Machín, A.; Cotto, M.; Duconge, J.; Arango, J.C.; Morant, C.; Pinilla, S.; Soto-Vázquez, L.; Resto, E.; Márquez, F. Hydrogen Production via Water Splitting Using Different Au@ZnO Catalysts under UV–Vis Irradiation. *J. Photochem. Photobiol. A Chem.* **2018**, *353*, 385–394. [\[CrossRef\]](#)
11. Machín, A.; Arango, J.C.; Fontánez, K.; Cotto, M.; Duconge, J.; Soto-Vázquez, L.; Resto, E.; Petrescu, F.I.T.; Morant, C.; Márquez, F. Biomimetic Catalysts Based on Au@ZnO–Graphene Composites for the Generation of Hydrogen by Water Splitting. *Biomimetics* **2020**, *5*, 39. [\[CrossRef\]](#)
12. Bisaria, K.; Sinha, S.; Singh, R.; Iqbal, H.M.N. Recent Advances in Structural Modifications of Photo-Catalysts for Organic Pollutants Degradation—A Comprehensive Review. *Chemosphere* **2021**, *284*, 131263. [\[CrossRef\]](#)
13. Wang, H.; Hu, P.; Zhou, J.; Roeyfaers, M.B.J.; Weng, B.; Wang, Y.; Ji, H. Ultrathin 2D/2D Ti₃C₂T_x/Semiconductor Dual-Functional Photocatalysts for Simultaneous Imine Production and H₂ Evolution. *J. Mater. Chem. A* **2021**, *9*, 19984–19993. [\[CrossRef\]](#)
14. Qiu, Q.; Zhu, P.; Liu, Y.; Liang, T.; Xie, T.; Lin, Y. Highly Efficient In₂S₃/WO₃ Photocatalysts: Z-Scheme Photocatalytic Mechanism for Enhanced Photocatalytic Water Pollutant Degradation under Visible Light Irradiation. *RSC Adv.* **2021**, *11*, 3333–3341. [\[CrossRef\]](#)
15. Duan, X.; Yang, J.; Hu, G.; Yang, C.; Chen, Y.; Liu, Q.; Ren, S.; Li, J. Optimization of TiO₂/ZSM-5 Photocatalysts: Energy Band Engineering by Solid State Diffusion Method with Calcination. *J. Environ. Chem. Eng.* **2021**, *9*, 105563. [\[CrossRef\]](#)
16. Dharma, H.N.C.; Jaafar, J.; Widiastuti, N.; Matsuyama, H.; Rajabsadeh, S.; Othman, M.H.D.; Rahman, M.A.; Jafri, N.N.M.; Suhaimin, N.S.; Nasir, A.M.; et al. A Review of Titanium Dioxide (TiO₂)-Based Photocatalyst for Oilfield-Produced Water Treatment. *Membranes* **2022**, *12*, 345. [\[CrossRef\]](#)
17. Xia, C.; Nguyen, T.H.C.; Nguyen, X.C.; Kim, S.Y.; Nguyen, D.L.T.; Raizada, P.; Singh, P.; Nguyen, V.-H.; Nguyen, C.C.; Hoang, V.C.; et al. Emerging Cocatalysts in TiO₂-Based Photocatalysts for Light-Driven Catalytic Hydrogen Evolution: Progress and Perspectives. *Fuel* **2022**, *307*, 121745. [\[CrossRef\]](#)
18. Tang, R.; Gong, D.; Deng, Y.; Xiong, S.; Deng, J.; Li, L.; Zhou, Z.; Zheng, J.; Su, L.; Yang, L. π - π Stacked Step-Scheme PDI/g-C₃N₄/TiO₂@Ti₃C₂ Photocatalyst with Enhanced Visible Photocatalytic Degradation towards Atrazine via Peroxymonosulfate Activation. *Chem. Eng. J.* **2022**, *427*, 131809. [\[CrossRef\]](#)
19. Danfá, S.; Oliveira, C.; Santos, R.; Martins, R.C.; Quina, M.M.J.; Gomes, J. Development of TiO₂-Based Photocatalyst Supported on Ceramic Materials for Oxidation of Organic Pollutants in Liquid Phase. *Appl. Sci.* **2022**, *12*, 7941. [\[CrossRef\]](#)
20. Machín, A.; Soto-Vázquez, L.; Colón-Cruz, C.; Valentín-Cruz, C.A.; Claudio-Serrano, G.J.; Fontánez, K.; Resto, E.; Petrescu, F.I.; Morant, C.; Márquez, F. Photocatalytic Activity of Silver-Based Biomimetics Composites. *Biomimetics* **2021**, *6*, 4. [\[CrossRef\]](#)
21. Al Jitan, S.; Li, Y.; Bahamon, D.; Žerjav, G.; Tatiparthi, V.S.; Aubry, C.; Sinnokrot, M.; Matouk, Z.; Rajput, N.; Gutierrez, M.; et al. Unprecedented Photocatalytic Conversion of Gaseous and Liquid CO₂ on Graphene-Impregnated Pt/Cu-TiO₂. *SSRN J.* **2022**. [\[CrossRef\]](#)
22. Li, B.; Ding, Y.; Li, Q.; Guan, Z.; Zhang, M.; Yang, J. The Photothermal Effect Enhance Visible Light-Driven Hydrogen Evolution Using Urchin-like Hollow RuO₂/TiO₂/Pt/C Nanomaterial. *J. Alloys Compd.* **2022**, *890*, 161722. [\[CrossRef\]](#)
23. Rashid, M.M.; Simončič, B.; Tomšič, B. Recent Advances in TiO₂-Functionalized Textile Surfaces. *Surf. Interfaces* **2021**, *22*, 100890. [\[CrossRef\]](#)
24. Nguyen, T.T.; Cao, T.M.; Balayeva, N.O.; Pham, V.V. Thermal Treatment of Polyvinyl Alcohol for Coupling MoS₂ and TiO₂ Nanotube Arrays toward Enhancing Photoelectrochemical Water Splitting Performance. *Catalysts* **2021**, *11*, 857. [\[CrossRef\]](#)
25. Maver, K.; Arçon, I.; Fanetti, M.; Al Jitan, S.; Palmisano, G.; Valant, M.; Štangar, U.L. Improved Photocatalytic Activity of SnO₂-TiO₂ Nanocomposite Thin Films Prepared by Low-Temperature Sol-Gel Method. *Catal. Today* **2022**, *397–399*, 540–549. [\[CrossRef\]](#)
26. Li, Z.; Li, H.; Wang, S.; Yang, F.; Zhou, W. Mesoporous Black TiO₂/MoS₂/Cu₂S Hierarchical Tandem Heterojunctions toward Optimized Photothermal-Photocatalytic Fuel Production. *Chem. Eng. J.* **2022**, *427*, 131830. [\[CrossRef\]](#)
27. Wang, P.; Yuan, Y.; Liu, Q.; Cheng, Q.; Shen, Z.; Yu, Z.; Zou, Z. Solar-Driven Lignocellulose-to-H₂ Conversion in Water Using 2D-2D MoS₂/TiO₂ Photocatalysts. *ChemSusChem* **2021**, *14*, 2860–2865. [\[CrossRef\]](#)
28. Machín, A.; Fontánez, K.; Duconge, J.; Cotto, M.C.; Petrescu, F.I.; Morant, C.; Márquez, F. Photocatalytic Degradation of Fluoroquinolone Antibiotics in Solution by Au@ZnO-rGO-GC₃N₄ Composites. *Catalysts* **2022**, *12*, 166. [\[CrossRef\]](#)
29. He, Z.; Cai, Q.; Fang, H.; Situ, G.; Qiu, J.; Song, S.; Chen, J. Photocatalytic Activity of TiO₂ Containing Anatase Nanoparticles and Rutile Nanoflower Structure Consisting of Nanorods. *J. Environ. Sci.* **2013**, *25*, 2460–2468. [\[CrossRef\]](#)
30. Soni, S.; Chouhan, N.; Meena, R.K.; Kumar, S.; Dalela, B.; Mishra, M.; Meena, R.S.; Gupta, G.; Kumar, S.; Alvi, P.A.; et al. Electronic Structure and Room Temperature Ferromagnetism in Gd-doped Cerium Oxide Nanoparticles for Hydrogen Generation via Photocatalytic Water Splitting. *Glob. Chall.* **2019**, *3*, 1800090. [\[CrossRef\]](#)
31. Kong, D.; He, H.; Song, Q.; Wang, B.; Lv, W.; Yang, Q.-H.; Zhi, L. Rational Design of MoS₂@graphene Nanocables: Towards High Performance Electrode Materials for Lithium Ion Batteries. *Energy Environ. Sci.* **2014**, *7*, 3320–3325. [\[CrossRef\]](#)

32. Wang, L.; Li, J.; Zhou, H.; Huang, Z.; Zhai, B.; Liu, L.; Hu, L. Three-Dimensionally Layers Nanosheets of MoS₂ with Enhanced Electrochemical Performance Using as Free-Standing Anodes of Lithium Ion Batteries. *J. Mater. Sci. Mater. Electron.* **2018**, *29*, 3110–3119. [\[CrossRef\]](#)
33. Vattikuti, S.V.P.; Shim, J. Synthesis, Characterization and Photocatalytic Performance of Chemically Exfoliated MoS₂. *IOP Conf. Ser. Mater. Sci. Eng.* **2018**, *317*, 012025. [\[CrossRef\]](#)
34. Jayakumar, G.; Irudayaraj, A.A.; Raj, A.D. Investigation on the Synthesis and Photocatalytic Activity of Activated Carbon–Cerium Oxide (AC–CeO₂) Nanocomposite. *Appl. Phys. A* **2019**, *125*, 742. [\[CrossRef\]](#)
35. Ederer, J.; Štátný, M.; Došek, M.; Henych, J.; Janoš, P. Mesoporous Cerium Oxide for Fast Degradation of Aryl Organophosphate Flame Retardant Triphenyl Phosphate. *RSC Adv.* **2019**, *9*, 32058–32065. [\[CrossRef\]](#)
36. Tamizhdurai, P.; Sakthinathan, S.; Chen, S.-M.; Shanthi, K.; Sivasanker, S.; Sangeetha, P. Environmentally Friendly Synthesis of CeO₂ Nanoparticles for the Catalytic Oxidation of Benzyl Alcohol to Benzaldehyde and Selective Detection of Nitrite. *Sci. Rep.* **2017**, *7*, 46372. [\[CrossRef\]](#)
37. Zhou, M.; Liu, Y.; Wu, B.; Zhang, X. Different Crystalline Phases of Aligned TiO₂ Nanowires and Their Ethanol Gas Sensing Properties. *Phys. E Low-Dimens. Syst. Nanostruct.* **2019**, *114*, 113601. [\[CrossRef\]](#)
38. Akita, A.; Kobayashi, H.; Tada, H. Action of Chloride Ions as a Habit Modifier in the Hydrothermal Crystal Growth of Rutile TiO₂ Nanorod from SnO₂ Seed Crystal. *Chem. Phys. Lett.* **2020**, *761*, 138003. [\[CrossRef\]](#)
39. *The International Center for Diffraction Data (ICDD) No. 00-004-0784*; ICDD: Newtown Square, PA, USA, 2008.
40. Wieting, T.J.; Verble, J.L. Infrared and Raman Studies of Long-Wavelength Optical Phonons in Hexagonal MoS₂. *Phys. Rev. B* **1971**, *3*, 4286–4292. [\[CrossRef\]](#)
41. Li, H.; Zhang, Q.; Yap, C.C.R.; Tay, B.K.; Edwin, T.H.T.; Olivier, A.; Baillargeat, D. From Bulk to Monolayer MoS₂: Evolution of Raman Scattering. *Adv. Funct. Mater.* **2012**, *22*, 1385–1390. [\[CrossRef\]](#)
42. Castellanos-Gomez, A.; Quereda, J.; van der Meulen, H.P.; Agraït, N.; Rubio-Bollinger, G. Spatially Resolved Optical Absorption Spectroscopy of Single- and Few-Layer MoS₂ by Hyperspectral Imaging. *Nanotechnology* **2016**, *27*, 115705. [\[CrossRef\]](#) [\[PubMed\]](#)
43. Jayakumar, G.; Albert Irudayaraj, A.; Dhayal Raj, A. A Comprehensive Investigation on the Properties of Nanostructured Cerium Oxide. *Opt. Quant. Electron.* **2019**, *51*, 312. [\[CrossRef\]](#)
44. Dos Santos, M.L.; Lima, R.C.; Riccardi, C.S.; Tranquilin, R.L.; Bueno, P.R.; Varela, J.A.; Longo, E. Preparation and Characterization of Ceria Nanospheres by Microwave-Hydrothermal Method. *Mater. Lett.* **2008**, *62*, 4509–4511. [\[CrossRef\]](#)
45. Cui, J.; Hope, G.A. Raman and Fluorescence Spectroscopy of CeO₂, Er₂O₃, Nd₂O₃, Tm₂O₃, Yb₂O₃, La₂O₃, and Tb₄O₇. *J. Spectrosc.* **2015**, *2015*, 940172. [\[CrossRef\]](#)
46. Bharti, B.; Kumar, S.; Lee, H.-N.; Kumar, R. Formation of Oxygen Vacancies and Ti³⁺ State in TiO₂ Thin Film and Enhanced Optical Properties by Air Plasma Treatment. *Sci. Rep.* **2016**, *6*, 32355. [\[CrossRef\]](#)
47. Ma, R.; Islam, M.J.; Reddy, D.A.; Kim, T.K. Transformation of CeO₂ into a Mixed Phase CeO₂/Ce₂O₃ Nanohybrid by Liquid Phase Pulsed Laser Ablation for Enhanced Photocatalytic Activity through Z-Scheme Pattern. *Ceram. Int.* **2016**, *42*, 18495–18502. [\[CrossRef\]](#)
48. Briggs, D.; Seah, M. *Practical Surface Analysis*; Wiley: New York, NY, USA, 1994.
49. Pal, P.; Pahari, S.K.; Sinhamahapatra, A.; Jayachandran, M.; Kiruthika, G.V.M.; Bajaj, H.C.; Panda, A.B. CeO₂ Nanowires with High Aspect Ratio and Excellent Catalytic Activity for Selective Oxidation of Styrene by Molecular Oxygen. *RSC Adv.* **2013**, *3*, 10837. [\[CrossRef\]](#)
50. Ma, J.; Xing, M.; Yin, L.; San Hui, K.; Hui, K.N. Porous Hierarchical TiO₂/MoS₂/rGO Nanoflowers as Anode Material for Sodium Ion Batteries with High Capacity and Stability. *Appl. Surf. Sci.* **2021**, *536*, 147735. [\[CrossRef\]](#)
51. Makuła, P.; Pacia, M.; Macyk, W. How To Correctly Determine the Band Gap Energy of Modified Semiconductor Photocatalysts Based on UV–Vis Spectra. *J. Phys. Chem. Lett.* **2018**, *9*, 6814–6817. [\[CrossRef\]](#)
52. Fonseca-Cervantes, O.R.; Pérez-Larios, A.; Romero Arellano, V.H.; Sulbaran-Rangel, B.; Guzmán González, C.A. Effects in Band Gap for Photocatalysis in TiO₂ Support by Adding Gold and Ruthenium. *Processes* **2020**, *8*, 1032. [\[CrossRef\]](#)
53. Saha, D.; Kruse, P. Editors' Choice—Review—Conductive Forms of MoS₂ and Their Applications in Energy Storage and Conversion. *J. Electrochem. Soc.* **2020**, *167*, 126517. [\[CrossRef\]](#)
54. Amendola, V.; Pilot, R.; Frascioni, M.; Maragò, O.M.; Iatì, M.A. Surface Plasmon Resonance in Gold Nanoparticles: A Review. *J. Phys. Condens. Matter* **2017**, *29*, 203002. [\[CrossRef\]](#) [\[PubMed\]](#)
55. Yonggang, L.; Yingzhen, Z.; Zengxing, L.; Shen, X.; Jianying, H.; Kim, H.N.; Yuekun, L. Molybdenum Sulfide Cocatalyst Activation upon Photodeposition of Cobalt for Improved Photocatalytic Hydrogen Production Activity of ZnCdS. *Chem. Eng. J.* **2021**, *425*, 131478. [\[CrossRef\]](#)
56. Dung, V.D.; Thuy, T.D.N.; Periyayya, U.; Yeong-Hoon, C.; Gyu-Cheol, K.; Jin-Kyu, Y.; Duy-Thanh, T.; Thanh Duc, L.; Hyuk, C.; Hyun You, K.; et al. Insightful Understanding of Hot-carrier Generation and Transfer in Plasmonic Au@CeO₂ Core–Shell Photocatalysts for Light-Driven Hydrogen Evolution Improvement. *App. Catal. B Environ.* **2021**, *286*, 119947. [\[CrossRef\]](#)
57. Rusinque, B.; Escobedo, S.; de Lasa, H. Hydrogen Production via Pd–TiO₂ Photocatalytic Water Splitting under Near-UV and Visible Light: Analysis of the Reaction Mechanism. *Catalysts* **2021**, *11*, 405. [\[CrossRef\]](#)

58. Chengzhang, Z.; Yuting, W.; Zhifeng, J.; Fanchao, X.; Qiming, X.; Cheng, S.; Qing, T.; Weixin, Z.; Xiaoguang, D.; Shaobin, W. CeO₂ Nanocrystal-modified Layered MoS₂/g-C₃N₄ as 0D/2D Ternary Composite for Visible-Light Photocatalytic Hydrogen Evolution: Interfacial Consecutive Multi-Step Electron Transfer and Enhanced H₂O Reactant Adsorption. *Appl. Catal. B Environ.* **2019**, *259*, 118072. [\[CrossRef\]](#)
59. Donghyung, K.; Kijung, Y. Boron Doping Induced Charge Transfer Switching of a C₃N₄/ZnO Photocatalyst from Z-Scheme to Type II to Enhance Photocatalytic Hydrogen Production. *Appl. Catal. B Environ.* **2021**, *282*, 119538. [\[CrossRef\]](#)
60. Bashiri, R.; Irfan, M.S.; Mohamed, N.M.; Sufian, S.; Ling, L.Y.; Suhaimi, N.A.; Samsudin, M.F.R. Hierarchically SrTiO₃@TiO₂@Fe₂O₃ Nanorod Heterostructures for Enhanced Photoelectrochemical Water Splitting. *Int. J. Hydrogen Energy* **2021**, *46*, 24607–24619. [\[CrossRef\]](#)
61. Tian, Y.; Yang, X.; Li, L.; Zhu, Y.; Wu, Q.; Li, Y.; Ma, F.; Yu, Y. A Direct Dual Z-scheme 3DOM SnS₂–ZnS/ZrO₂ Composite with Excellent Photocatalytic Degradation and Hydrogen Production Performance. *Chemosphere* **2021**, *279*, 130882. [\[CrossRef\]](#)
62. Ma, B.; Bi, J.; Lv, J.; Kong, C.; Yan, P.; Zhao, X.; Zhang, X.; Yang, T.; Yang, Z. Inter-Embedded Au-Cu₂O Heterostructure for the Enhanced Hydrogen Production from Water Splitting under the Visible Light. *Chem. Eng. J.* **2021**, *41*, 126709. [\[CrossRef\]](#)
63. Jourshabani, M.; Shariatnia, Z.; Badiei, A. Synthesis and Characterization of Novel Sm₂O₃/S-Doped g-C₃N₄ Nanocomposites with Enhanced Photocatalytic Activities under Visible Light Irradiation. *Appl. Surf. Sci.* **2018**, *427*, 375–387. [\[CrossRef\]](#)
64. Prabavathi, S.L.; Saravanakumar, K.; Nkambule, T.T.I.; Muthuraj, V.; Mamba, G. Enhanced Photoactivity of Cerium Tungstate-Modified Graphitic Carbon Nitride Heterojunction Photocatalyst for the Photodegradation of Moxifloxacin. *J. Mater. Sci. Mater. Electron.* **2020**, *31*, 11434–11447. [\[CrossRef\]](#)
65. Cao, J.; Li, X.; Lin, H.; Chen, S.; Fu, X. In Situ Preparation of Novel p–n Junction Photocatalyst BiOI/(BiO)₂CO₃ with Enhanced Visible Light Photocatalytic Activity. *J. Hazard. Mater.* **2012**, *239–240*, 316–324. [\[CrossRef\]](#)
66. Nethercot, A.H. Prediction of Fermi Energies and Photoelectric Thresholds Based on Electronegativity Concepts. *Phys. Rev. Lett.* **1974**, *33*, 1088–1091. [\[CrossRef\]](#)
67. Kutchinsky, J.; Taboryski, R.; Sørensen, C.B.; Hansen, J.B.; Lindelof, P.E. Experimental Investigation of Supercurrent Enhancement in S–N–S Junctions by Non-Equilibrium Injection into Supercurrent-Carrying Bound Andreev States. *Phys. C Supercond.* **2001**, *352*, 4–10. [\[CrossRef\]](#)
68. Elaziouti, A.; Laouedj, N.; Bekka, A.; Vannier, R.-N. Preparation and Characterization of p–n Heterojunction CuBi₂O₄/CeO₂ and Its Photocatalytic Activities under UVA Light Irradiation. *J. King Saud Univ. Sci.* **2015**, *27*, 120–135. [\[CrossRef\]](#)
69. Lin, Y.; Ren, P.; Wei, C. Fabrication of MoS₂/TiO₂ Heterostructures with Enhanced Photocatalytic Activity. *CrystEngComm* **2019**, *21*, 3439–3450. [\[CrossRef\]](#)
70. Soto-Vázquez, L.; Rolón-Delgado, F.; Rivera, K.; Cotto, M.C.; Ducongé, J.; Morant, C.; Pinilla, S.; Márquez-Linares, F.M. Catalytic Use of TiO₂ Nanowires in the Photodegradation of Benzophenone-4 as an Active Ingredient in Sunscreens. *J. Environ. Manag.* **2019**, *247*, 822–828. [\[CrossRef\]](#)

Disclaimer/Publisher's Note: The statements, opinions and data contained in all publications are solely those of the individual author(s) and contributor(s) and not of MDPI and/or the editor(s). MDPI and/or the editor(s) disclaim responsibility for any injury to people or property resulting from any ideas, methods, instructions or products referred to in the content.